
SLoRD: Structural Low-Rank Descriptors for Shape Consistency in Vertebrae Segmentation

Xin You^{1,2}, Yixin Lou^{1,2}, Minghui Zhang^{1,2}, Chuyan Zhang^{1,2}, Jie Yang^{1,2}, Yun Gu^{1,2*}

¹Institute of Medical Robotics, Shanghai Jiao Tong University, Shanghai, China

²Institute of Image Processing and Pattern Recognition, Department of Automation, Shanghai Jiao Tong University, Shanghai, China
{sjtu_youxin, geron762}@sjtu.edu.cn

Abstract

Automatic and precise segmentation of vertebrae from CT images is crucial for various clinical applications. However, due to a lack of explicit and strict constraints, existing methods especially for single-stage methods, still suffer from the challenge of intra-vertebrae segmentation inconsistency, which refers to multiple label predictions inside a singular vertebra. For multi-stage methods, vertebrae detection serving as the first step, is affected by the pathology and mental implants. Thus, incorrect detections cause biased patches before segmentation, then lead to inconsistent labeling and segmentation. In our work, motivated by the perspective of instance segmentation, we try to label individual and complete binary masks to address this limitation. Specifically, a contour-based network is proposed based on Structural Low-Rank Descriptors for shape consistency, termed SLoRD. These contour descriptors are acquired in a data-driven manner in advance. For a more precise representation of contour descriptors, we adopt the spherical coordinate system and devise the spherical centroid. Besides, the contour loss is designed to impose explicit consistency constraints, facilitating regressed contour points close to vertebral boundaries. Quantitative and qualitative evaluations on VerSe 2019 demonstrate the superior performance of our framework over other single-stage and multi-stage state-of-the-art (SOTA) methods. Source codes are available <https://github.com/AlexYouXin/SLoRD-VerSe>.

1 Introduction

Automatic segmentation of vertebrae from CT images plays a significant role in spinal disease treatment, including preoperative diagnosis, surgical guidance, and postoperative assessment [1–3]. Moreover, the shape analysis of vertebrae serves as an important anatomical reference for other anatomies in clinical practices [4, 5]. According to the anatomical prior of vertebral structures, it is emerging to preserve the consistency of label predictions inside a singular vertebra [6]. However, as illustrated in Figure 1, for single-stage and multi-stage methods, predicted masks for the specific vertebra might contain inconsistent label predictions, and partial voxel predictions in adjacent vertebrae reveal the same label. That phenomenon has been recognized as intra-vertebrae label inconsistency [7], which poses a large challenge for the task of vertebrae segmentation.

Specifically, earlier methods solved vertebrae segmentation from CT images by employing statistical models [8], active shape models [9], level sets [10] and graph cuts theories [11]. However, those approaches fail to generalize well on unseen data. Recent deep learning-based methods demonstrate a more promising performance for vertebrae image segmentation even with arbitrary FOVs. One category of existing works [1, 12, 7] adopted single-stage models. Lessmann et al. [1] used fully convolutional networks by iteratively analyzing image patches for automatic vertebrae segmentation

*Corresponding Author

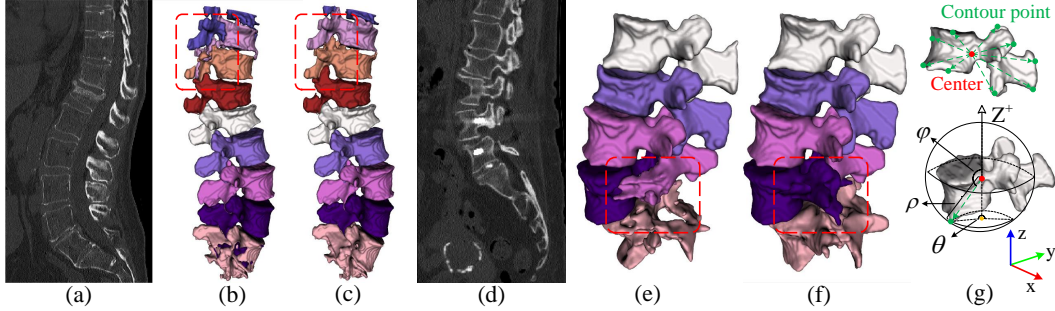


Figure 1: (a) CT case 1. (b-c) Coarse prediction by MedNeXt [22] & refined outcome by MedNeXt + SLoRD on case 1. (d) Case 2 with meta artifacts. (e-f) Coarse prediction by the multi-stage pipeline Spine-Transformer [15] & our refined prediction on case 2. (g) Spherical coordinate system for 3D vertebral contour descriptions. x , y and z axis represent voxel orientations from Right/Anterior/Inferior to Left/Posterior/Superior. ρ : the radial distance away from the spherical center, ϕ : the polar angle between the radial vector and z^+ , θ : the azimuth angle between x^+ and the projected radial vector in the XOY plane.

and identification. However, this method relies on the perfect prediction for the first label and hardly recovers from failures in the top vertebra. You et al. [7] proposed an edge detection block to restrain boundaries for better consistency inside the boundary box. However, these models still suffer from drawbacks of similar appearances between adjacent vertebrae and the patch-based inference paradigm, resulting in intra-vertebrae label inconsistency. The other methods [13–16] designed a multi-stage pipeline to improve the segmentation performance. Tao et al. [15] introduced a Transformer to handle the labeling task, then employed 3D UNet [17] with the original CT image and an auxiliary heatmap as inputs to segment all vertebrae. Besides, Payer et al. [16] implemented a three-step approach to first localize the spine, then simultaneously located and identified each vertebra, and finally segmented each vertebra. However, a biased detected patch due to the inaccurate center regression will enforce inconsistency inside vertebrae, particularly for pathological vertebrae with abnormal shapes or mental implants as illustrated by Figure 1(d & e). Also, this limitation can be referred to according to the qualitative analysis of experimental results in [15].

Carrying out the cause and effect analysis, we summarize three leading factors contributing to the intra-vertebrae segmentation inconsistency for CT images. ❶ Neighbored vertebrae show similar appearances and intensity values from CT images, which results in label confusion between adjacent vertebrae [18]. ❷ Vertebrae CT scans display arbitrary field-of-views (FOVs) with various label distributions [19]. Consequently, U-shape networks [20, 21] suffer from a poor identification of the spine, especially for bi-terminal vertebrae [7]. ❸ A portion of spines bear pathological vertebrae with abnormal or deformed shapes [13]. And there also exist metal artifacts in some CT scans. In brief, vertebral data show different characteristics from other anatomical structures, making it difficult to precisely and consistently segment vertebrae with sequential labels.

Essentially, all the methods above do not impose explicit and strict constraints for voxels inside each vertebra during training, resulting in label inconsistency. To address this challenge, motivated by the concept of instance segmentation [1], we attempt to label individual and complete binary masks to achieve multi-label vertebrae segmentation. Due to the connection between superior and inferior articular processes [2], the main challenge transforms to how to divide joint binary vertebral masks without destroying original contours. Thus, we devise an effective contour-based network based on Structural Low-Rank Descriptors for shape consistency, termed SLoRD. Specifically, vertebrae show similar 3D shapes according to anatomical structures, lumbar and thoracic vertebrae in particular. Hence, we can find out a low-dimension contour space to represent all vertebrae data. Intuited by [23], we build a novel representation way of contours based on the spherical coordinate system as shown in Figure 1(g). Additionally, spherical centroids are proposed to enhance the precision of contour representation vectors. Via a linear combination between basic vectors of the contour space, instance masks of vertebrae can be approximately restored. Then vertebral labels provided by coarse predictions facilitate the generation of semantic masks. Finally, we incorporate this pipeline into deep neural networks to boost the framework’s generalization abilities on unseen datasets. And a contour loss is devised to exert a consistency constraint for each vertebra. Extensive experiments are carried out on the public VerSe 2019 dataset [18]. And our method achieves SOTA performance compared

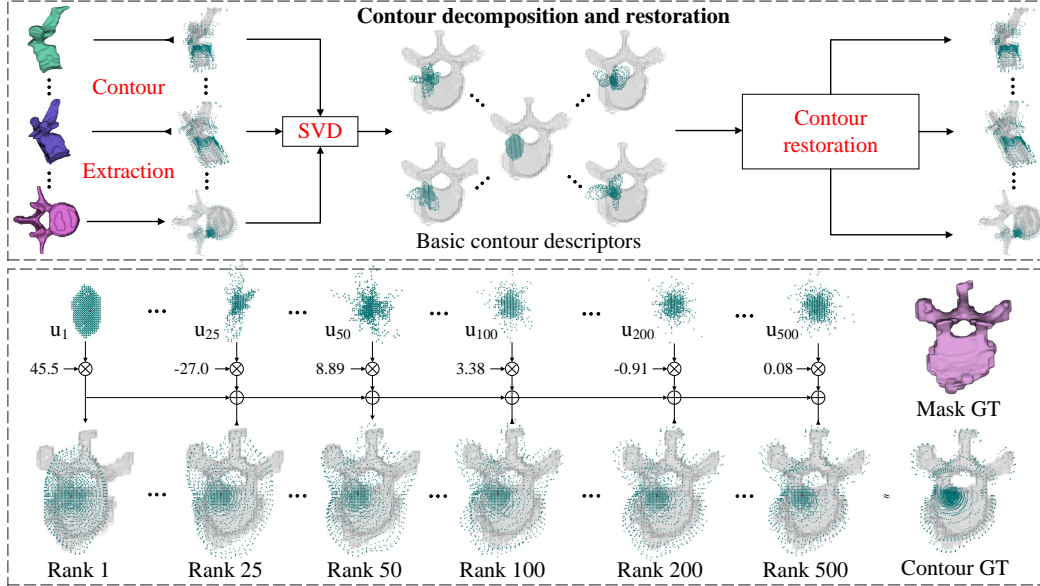


Figure 2: Upper: The flow of contour decomposition and restoration. Lower: The linear combination process between basic contour descriptors. The first row indicates basic descriptors of specific ranks. The second row refers to weighted visualizations.

with other single-stage and multi-stage approaches. Moreover, qualitative results demonstrate that our two-stage pipeline can significantly improve the intra-vertebrae segmentation inconsistency.

2 Methodology

2.1 Preliminaries on Contour Descriptors

For designing contour descriptors, we incorporate the idea from PolarMask [23, 24], in which each contour point is encoded with the polar coordinate. Specifically, the origin point is set as the centroid of the object, and each contour point is determined by the fixed sampling angle and corresponding distance. Directional angles from 0° to 360° efficiently connect each point into a complete contour. To strike a balance between the precision and computational cost, the polar system makes good use of the non-convex shape property of vertebrae anatomies and chooses the maximum distance at the same angle.

Since it is challenging to extend the polar system to contour representations of 3D objects like vertebrae, we formulate contours with the spherical coordinate system as shown in Figure 1(g). With respect to the inner centroid, we describe the boundary using spherical coordinates $(\rho_{ij}, \theta_i, \phi_j)$, $i = 1, \dots, I; j = 1, \dots, J$. Here ρ represents the length of the radial vector from the spherical center to the contour point, ϕ is the polar angle between the radial vector and z^+ , θ means the azimuth angle between x^+ and the projected radial vector in the XOY plane. Angular coordinates θ_i, ϕ_j are sampled uniformly with a sampling interval of 5° , with I equal to $\frac{360^\circ}{5^\circ} = 72$, J equal to $(\frac{180^\circ}{5^\circ} + 1) = 37$. Thus, given the sampling angle grid, only radial coordinates are recorded to represent the contour:

$$\boldsymbol{\rho} = [\rho_{11}, \dots, \rho_{1J}, \dots, \rho_{I1}, \dots, \rho_{IJ}]^T \quad (1)$$

Here $\boldsymbol{\rho}$ refers to the contour descriptor, with the dimension N equal to $I \times J = 2664$. Since shapes of most vertebrae are well structured and resembling to each other, low-rank contour descriptors can be exploited in a data-driven manner via Singular Value Decomposition (SVD) [24]. Detailedly, a non-convex contour matrix $\mathcal{M} = [\boldsymbol{\rho}_1, \dots, \boldsymbol{\rho}_L]$ is constructed from L vertebrae in the training data. Then we perform SVD on matrix \mathcal{M} :

$$\mathcal{M} = \mathbf{U} \boldsymbol{\Sigma} \mathbf{V}^T \quad (2)$$

Where $\mathbf{U}^{N \times N} = [\mathbf{u}_1, \dots, \mathbf{u}_N]$ and $\mathbf{V}^{L \times L} = [\mathbf{v}_1, \dots, \mathbf{v}_L]$ are orthogonal matrixes and $\boldsymbol{\Sigma}^{N \times L}$ is a rectangular diagonal matrix, consisting of singular values $[\sigma_1, \dots, \sigma_r]$ ($r = \min(N, L)$). The best

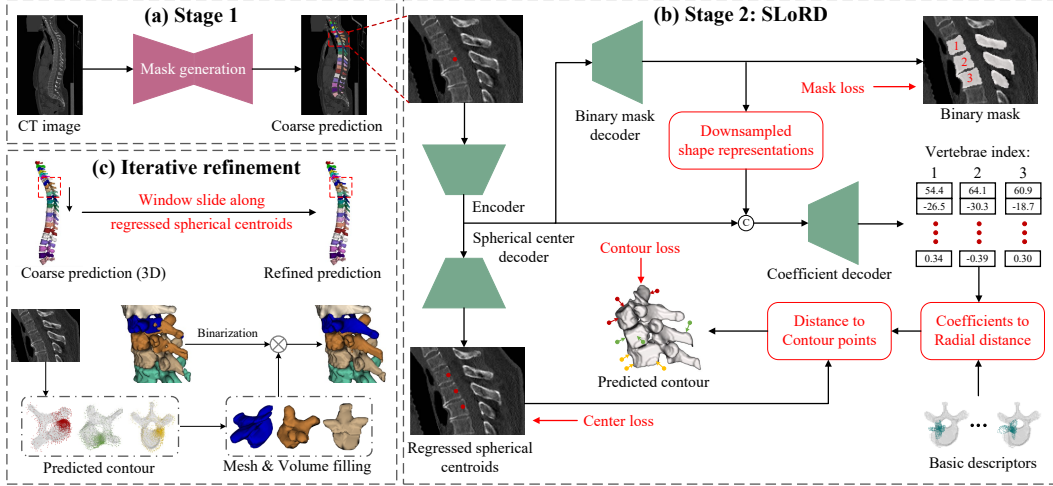


Figure 3: The two-stage framework. (a) Coarse predictions by arbitrary segmentation networks. (b) Based on the combination of basic contour descriptors, SLoRD aims to regress contour points close to vertebral boundaries. (c) Iterative refinement for coarse masks.

rank- k approximation of \mathcal{M} can be calculated as follows:

$$\mathcal{M}(k) = \sigma_1 \mathbf{u}_1 \mathbf{v}_1^T + \dots + \sigma_k \mathbf{u}_k \mathbf{v}_k^T = [\mathbf{u}_1, \dots, \mathbf{u}_k] \mathcal{C} = \mathbf{U}(k) \mathcal{C} \approx \mathcal{M} \quad (3)$$

$$\mathcal{C} = [\sigma_1 \mathbf{v}_1, \dots, \sigma_k \mathbf{v}_k]^T = \mathbf{U}(k)^T \mathcal{M} \quad (4)$$

Here $\mathbf{U}(k)^{N \times k}$ refers to k basic contour descriptors, which can span into the contour space and be acquired from the training data in advance. $\mathcal{C}^{k \times L}$ means combinational coefficients, calculated by eigen descriptors and matrix \mathcal{M} . As long as \mathcal{C} is correct, we can restore the original contours of vertebrae approximately as illustrated by Figure 2. For a better trade-off between performance and efficiency, only the first 200 basic contour descriptors are adopted in our work.

2.2 Spherical Centroid

Although the encoding scheme for vertebral contours is efficient, it is very tricky to determine the spherical center, which will significantly affect the restoration performance of vertebral shapes. Since the polar angle ϕ and azimuth angle θ are both sampled at equal intervals, a spherical center with a biased location will result in fewer sampling contour points for the boundary region far from it. Consequently, that region suffers from a contour under-representation. Hence, it has been a crucial topic on how to designate the spherical center.

A simple configuration is each vertebral centroid, averaged on both the vertebral body and spinous process. However, the centroid is acquired ignoring the optimization objective of enforcing contour points close to the boundary \mathcal{B} . Thus, to achieve a finer contour representation for the anatomical structure of vertebrae, a distance-based center should be marked by minimizing the average Euclidean distance between this center and the whole boundary surface. We formulate the distance-based center called spherical centroid C_s based on Eq (6):

$$\mathcal{B} = \mathcal{F}(M) \setminus M \quad (5)$$

$$C_s = \arg \min_{c \in M} \left(\frac{1}{|\mathcal{B}|} \sum_{b \in \mathcal{B}} d(c, b) + \lambda \cdot d(c, \delta) \right), \text{ s.t. } \delta = \arg \max_{j \in \mathcal{B}} j_y \quad (6)$$

Where $\mathcal{F}(\cdot)$ represents the morphological dilation operation, M refers to the segmentation mask of each vertebral volume, the boundary map \mathcal{B} is the difference set between the dilated mask $\mathcal{F}(M)$ and the mask itself M . Besides, $d(\cdot)$ means the Euclidean distance. The first item in Eq (6) refers to the average distance from each boundary point b to the center $c \in \mathcal{P}$. Besides, considering the non-convex shape prior of the spinous process, we attempt to push the spherical centroid closer to it. That will enlarge the value range of θ and ϕ , then enhance the shape representations of the spinous process. That is why the second regularization term is incorporated, in which δ is the boundary point with the largest y -dimensional index. λ is a scaling parameter, empirically set as 0.005.

2.3 Contour Generation with Contour Priors

To precisely restore the contour, it is significant to accurately achieve the coefficient according to Eq (4). Besides, the contour generation requires the precise regression of spherical centers as described in Section 2.2. Thus, we devise the SLoRD framework by introducing the center decoder and coefficient decoder as shown in Figure 3(b). The ground truth of centers C_s can be attained by Eq (6). And we employ the L_2 norm to regularize regressed centers \hat{C} , with the center loss \mathcal{L}_{center} equal to $\|C_s - \hat{C}\|^2$.

The direct loss regularization for combinational coefficients like the previous work [24] cannot work in this task. We reckon that phenomenon results from the magnitude difference between different dimensions of coefficient vectors and the magnitude variance between combinational coefficients from the same dimension. Thus, we transform coefficients into the radial distance with data-driven contour priors, then into the contour point cloud [25] centered at spherical centroids. After that, an explicit contour constraint $\mathcal{L}_{contour}$ is devised based on the average minimal distance from the contour point set \mathcal{P}_c to the boundary interface \mathcal{B} as illustrated by the following formula:

$$\mathcal{L}_{contour} = \frac{1}{|\mathcal{P}_c|} \sum_{p \in \mathcal{P}_c} \min_{b \in \mathcal{B}} d(p, b) \quad (7)$$

Where $|\mathcal{P}_c|$ means the voxel number of \mathcal{P}_c . Besides, it might be confusing why we do not adopt a direct distance regularization on the regressed point clouds compared with ground truths. A comprehensible perspective is that the SLoRD network do not bear any perception ability to identify the sampled angle grid in the spherical coordinate system since no relevant angular priors are introduced. That is why basic contour descriptors encoded by the spherical coordinate system will boost the contour representation of vertebral anatomies.

To reduce computational costs, we uniformly sample $\frac{1}{3}$ boundary points from \mathcal{B} to calculate the contour loss. Besides, an additional binary mask supervision \mathcal{L}_{mask} (cross-entropy loss plus Dice loss) will enforce an implicit regularization to the coefficient decoder by introducing vertebral shape information. Thus, the total loss is defined as follows:

$$\mathcal{L} = \mathcal{L}_{mask} + \mathcal{L}_{center} + \mathcal{L}_{contour} \quad (8)$$

Furthermore, segmentation inconsistency tends to appear in a sequential of vertebrae as highlighted in Figure 1. Some poor predictions even depict wrong identifications for a series of vertebrae. Under this circumstance, the iterative refinement for one vertebra each time cannot address this type of failure cases, and that is why we attempt to handle three vertebrae with sequential labels once. Assuming that coarse predictions reveal satisfactory performance for the top two vertebrae, even with a moderate inconsistency, SLoRD can significantly boost segmentation results.

2.4 Inference

In the inference phase, the patch to be refined in SLoRD is cropped along each vertebral center from coarse predictions as shown in Figure 3(a). The SLoRD framework will first refine three spherical centers corresponding to sequential vertebrae according to the prediction of the center decoder. Then the coefficient branch will output $3 \times N$ (N refers to the dimension of ρ) contour points surrounding three vertebral boundaries with different labels as revealed in Figure 3(c). After that, Marching Cube [26] is implemented to generate the triangle mesh, which is further voxelized into a filled volume [27]. After that, we perform the binarization on the coarse mask and multiply it with the filled volume to realize a refined mask with good label consistency and shape restoration via the auxiliary connected component analysis.

3 Experiment

3.1 Experimental Settings

Dataset. To evaluate the performance of our network, we conduct experiments on the challenging dataset [18]: MICCAI Challenge VerSe 2019, containing different pathological images. Specifically, VerSe 2019 consists of 160 spinal CT scans, which are split into 80/40/40 scans for training, public-test, and hidden-test cases in the first stage of generating coarse predictions. To ensure relatively

Table 1: Comparisons with other single-stage, two-stage and multi-stage methods on the public and hidden test datasets of VerSe 2019 (A-Dice: average Dice. M-Dice: median Dice. A-HD: average Hausdorff distance. M-HD: median Hausdorff distance).

Stage	Method	Public test				Hidden test			
		A-Dice \uparrow	M-Dice \uparrow	A-HD \downarrow	M-HD \downarrow	A-Dice \uparrow	M-Dice \uparrow	A-HD \downarrow	M-HD \downarrow
Single-stage	Lessmann N.[1]	85.08	94.25	8.58	4.62	85.76	93.86	8.20	5.38
	nnUNet [20]	85.81	92.55	12.50	10.25	86.59	92.62	12.78	12.00
	Verteformer [7]	86.39	91.22	11.14	10.28	86.54	90.74	10.55	10.51
	UNeXt[28]	83.80	85.20	18.63	13.51	83.36	88.39	12.19	11.77
	Swin UNETR [21]	85.42	90.57	16.01	12.55	83.46	88.91	16.03	13.58
	MedNeXt [22]	88.51	93.96	10.59	8.47	88.91	94.40	11.35	9.81
Multi-stage	Sekuboyina A. [18]	83.06	90.93	12.11	7.56	83.18	92.79	9.94	7.22
Multi-stage	Payer C. [16]	90.90	95.54	6.35	4.62	89.80	95.47	7.08	4.45
Multi-stage	Chen M. [18]	93.01	95.96	6.39	4.88	82.56	96.50	9.98	5.71
Two-stage	Tao R. [15]	90.49	94.26	6.53	4.31	89.94	94.01	6.96	4.73
Two-stage	Ours	90.94	95.08	6.14	4.74	90.87	95.90	6.53	4.25

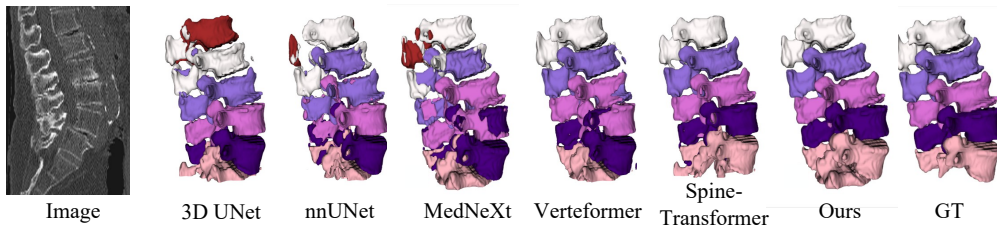


Figure 4: Qualitative visualizations of models in the benchmark.

fixed FOVs of iterative cropped patches in stage 2, we resample all data with a voxel space equal to $1.0 \times 1.0 \times 1.998mm^3$ in z, y, and x orientations. Then we select a size of $112 \times 128 \times 96$ to crop patches containing three sequential labeled vertebrae. And each patch is centered at the spherical centroid of the intermediate vertebra. To generate value variance in the center regression decoder, we exert a random translation on the patch center, with a range of $[-5, 5]$ on each coordinate dimension. And there are 113 cervical, 436 thoracic, 314 lumbar vertebrae respectively. For each middle vertebra, we repeat the translation process 3 times. Thus, there are a total of 2589 patches, which are split as 2100/489 cases for training and validation. During inference, the second-stage network is adopted to refine coarse predictions. Moreover, we choose the Dice score and Hausdorff distance (HD) as quantitative metrics [29].

Implementation Details. In stage 1, we choose MedNeXt as the baseline model, trained for 1000 epochs with $10.53M$ parameters. And we utilize a combination of cross entropy loss and Dice loss followed by [20]. The patch size is $128 \times 160 \times 96$. In stage 2, the refinement network is trained for 400 epochs, which employs the encoder of 3D UNet with only $5.15M$ parameters. And we utilize a weighted loss \mathcal{L}_{total} as illustrated in Section 2.3. We train all models using AdamW optimizer. With the linear warm-up strategy, the initial learning rate is set as $5e-4$ with a cosine learning rate decay scheduler, and weight decay is set as $1e-5$. The batch size is 2 and 16 for two stages individually. All models are implemented based on Pytorch and trained on 2 NVIDIA Tesla V100 GPUs.

3.2 Experimental Results

To evaluate the efficacy of our proposed method, we conduct qualitative and quantitative experimental results on VerSe 2019. As illustrated by Table 1, our method achieves SOTA performance on the average Dice and Hausdorff distance (HD) of the hidden test dataset compared with other single-stage and multi-stage methods. Specifically, our framework surpasses MedNeXt [22] (the best single-stage model) by 1.96% \uparrow average Dice score and $4.82mm \downarrow$ average Hausdorff distance. And these two metrics come to 0.93% \uparrow and $0.43mm \downarrow$ when compared with Spine-Transformer [15] (the best two-stage model), 8.31% \uparrow and $3.45mm \downarrow$ compared with Chen’s method [18] (the best multi-stage model). Moreover, the median Dice and HD of our method also reach a promising performance. Obviously, the superiority of segmentation performance originates from the consistency regularization generated by our instance-based SLoRD architecture. By labeling sequential instance masks, we will acquire semantic segmentation masks with better consistency.

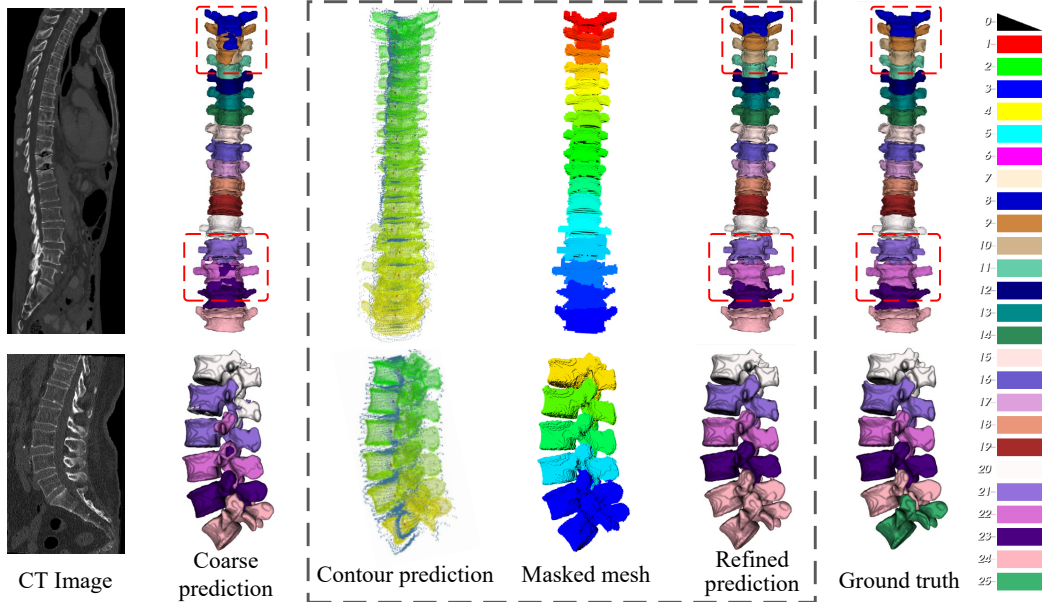


Figure 5: Visualizations of the detailed refinement process. Refined predictions in the dashed box reveal a better segmentation consistency in each vertebra compared with coarse predictions.

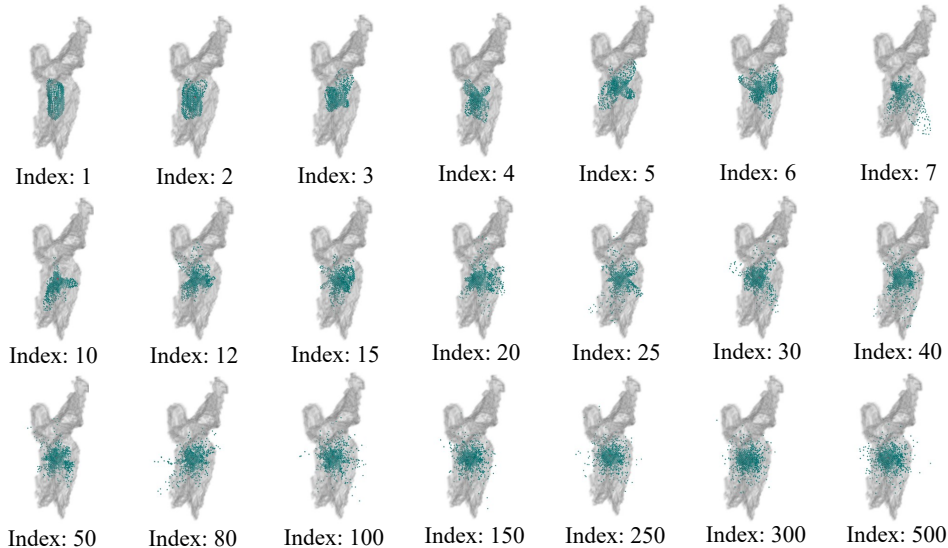


Figure 6: Visualizations of the decomposed contour descriptors. Different indexes refer to different contour vectors.

Qualitative visualizations are also displayed in Figure 1 and 4, which reveals that our framework could attain more consistent predictions in each vertebra even for challenging cases. As revealed in Figure 5, the whole refinement process is visualized. The results in the dashed box represent the efficacy of our proposed SLoRD. It is worth highlighting that each instance mask is generated via the linear combination of basic contour descriptors, which can be achieved in a data-driven manner. Here we give a depiction of decomposed contour priors by SVD as shown in Figure 6.

Besides, the efficiency analysis is conducted between our devised pipeline and other methods in the VerSe 2019 challenge. Specifically, we choose network parameters (M), computational costs (G FLOPs), and inference time per case (s) as quantitative metrics. As illustrated by Table 2, our

Table 2: Left: Ablation study on the plug-and-play property of SLoRD when applied to other CNNs and Transformer-based networks. Quantitative results on the hidden test dataset are provided. Right: The efficiency evaluation between our method and other multiple-stage approaches on the hidden test datasets of VerSe 2019.

Model	A-Dice	M-Dice	A-HD	M-HD	Method	Parameters (M)	FLOPs (G)	Inference speed (s)
nnUNet [20]	86.59	92.62	12.78	12.00	Verteformer [7]	330.65	336.5	65.2
nnUNet [20] + SLoRD	88.85	93.31	8.48	6.39	Payer C. [16]	34.33	517.6	260.0
Verteformer [7]	86.54	90.74	10.55	10.51	Tao R. [15]	38.41	631.3	176.3
Verteformer [7] + SLoRD	89.13	94.26	7.46	7.23	Ours	25.18	454.6	142.8

Table 3: Left: ablation study on the orientation of positive Z-axis, sampling interval, and the number of basic contour descriptors. Right: ablation study on the type of centers between the centroid and spherical center (ASD [29]: average surface distance).

(a) Ablation on the choice of positive Z-axis			
Settings	x-axis	y-axis	z-axis
ASD ↓	0.987±0.074	1.189±0.114	0.962±0.073
(b) Ablation on the sampling interval			
Settings	3°	5°	10°
ASD ↓	0.876±0.067	0.962±0.073	1.245±0.122
(c) Ablation on the rank number			
Settings	100	200	500
ASD ↓	1.033±0.080	0.962±0.073	0.917±0.068

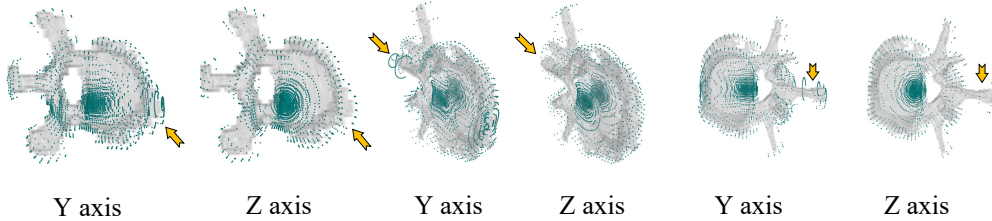
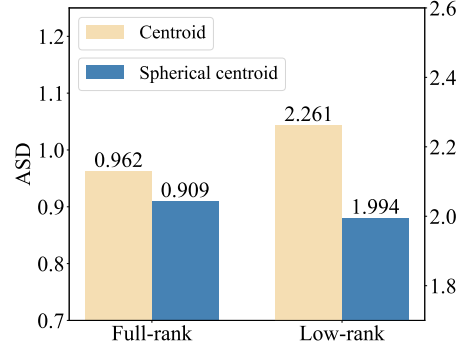


Figure 7: Visualizations of the full-rank contour restoration on the orientation setting of positive Z-axis in the spherical coordinate system. The voxel z axis from inferior to superior orientations is chosen as the final experimental setting.

approach only requires 25.18M network parameters, then achieves a 142.8s average inference time for each CT scan, which is much faster than Payer’s method (260.0s) and Tao’s method (176.3s).

3.3 Ablation Studies

In Table 3, we investigate a detailed ablation analysis on the contour representations based on the spherical coordinate system. For a simple yet effective evaluation, we adopt the average surface distance (ASD) between contour points and the boundary to assess the contour restoration performance. Here the ASD metric is calculated via the linear combination of full-rank contour descriptors by SVD. Thus, this distance value stands for the best performance that can be theoretically achieved due to the non-convex shape property of vertebral anatomies.

1) The orientation of the positive Z-axis: the voxel z-axis as the objective orientation achieves the lowest ASD value. Compared with the voxel y-axis, there is a 0.025 voxel distance drop. Besides, as revealed in Figure 7, there will be a deviation for contour points adjacent to the left and right ends of vertebrae. 2) The sampling interval of the polar angle ϕ and the azimuth angle θ : different values of the angular interval are considered. As shown in Table 3, a smaller interval means a denser sampling for the contour point cloud, which will inevitably promote the precision of regressed contours by SLoRD, and then elevate the final segmentation performance. Considering the computational efficiency, the hyper-parameter is specified as 5° , then the dimension N of each contour descriptor ρ is equal to $\frac{360^\circ}{5^\circ} \times (\frac{180^\circ}{5^\circ} + 1) = 2664$. 3) Spherical centroid vs. Centroid: adopting the spherical

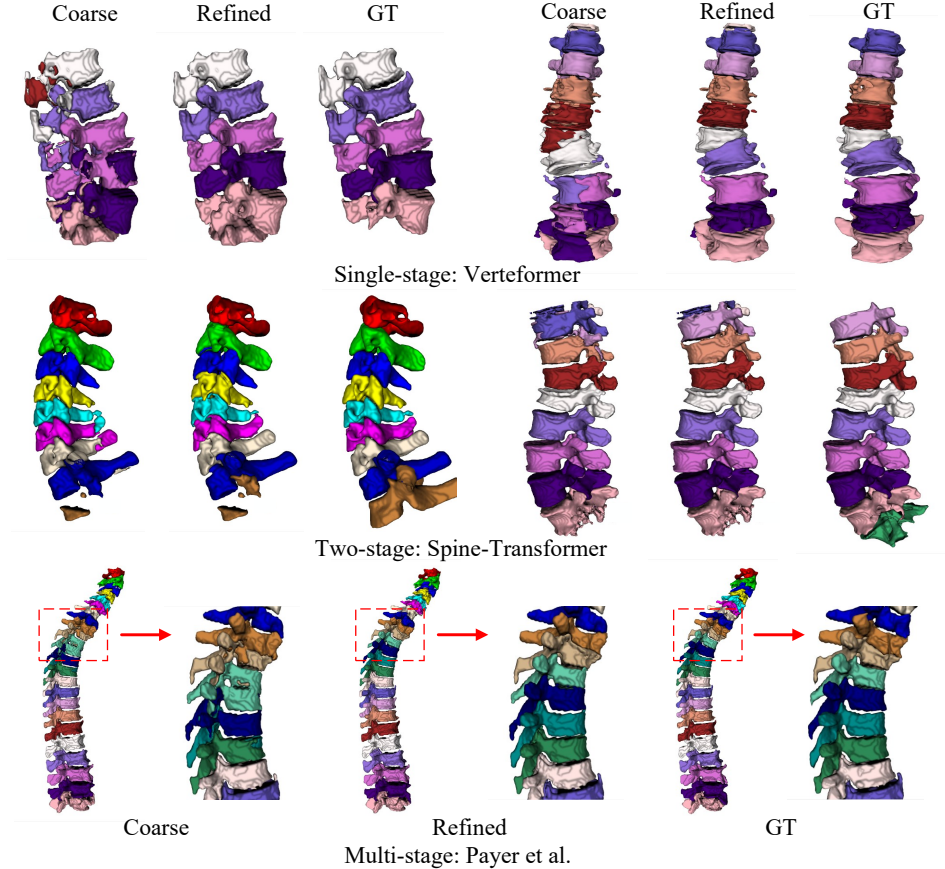


Figure 8: Improvement of our proposed SLoRD when applied to coarse predictions from other segmentation networks including the single-stage Verteformer [7], two-stage Spine-Transformer [15], and multi-stage Payer’s methods [18].

centroid reduces the ASD value [29] in low-rank and full-rank approximations, with a 0.053 and 0.267 decrease respectively. That demonstrates the advancement of spherical centroids owing to the optimization objective of its design.

We also carried out the ablation study on the plug-and-play property of SLoRD. For MedNeXt [22], the introduction of SLoRD brings remarkable gains on the segmentation performance of the public and hidden test datasets, with 2.43%, 1.96% Dice score increases and 4.45mm, 4.82mm HD decreases. Besides MedNeXt, our proposed SLoRD will boost segmentation networks including Verteformer [7], Spine-Transformer [15], [16] as shown in Table 2. Specifically, for Verteformer [7] which is aimed at the task of vertebrae segmentation, substantial improvements have been achieved on the average Dice score and HD (2.59% \uparrow , 3.09mm \downarrow). Detailed qualitative results are provided in Figure 8 to demonstrate the efficacy of SLoRD in promoting segmentation consistency when plugged into single-stage, two-stage, and multi-stage methods. As long as there is a satisfactory performance for the top two vertebrae, even with moderate inconsistency, SLoRD can significantly boost segmentation results.

4 Conclusion

In this paper, we address the challenge of intra-vertebrae segmentation inconsistency from the perspective of instance segmentation. Specifically, we propose a contour-based network to refine coarse predictions, based on the linear combination of structured vertebral contour descriptors. Besides, the proposed contour loss imposes consistency constraints, facilitating contour points close to vertebral boundaries. Detailed quantitative and qualitative results on VerSe 2019 have demonstrated the efficacy of our devised framework.

Acknowledgments

This work is supported in part by National Key R&D Program of China (2019YFB1311503), the Shanghai Sailing Program (20YF1420800), the Shanghai Health and Family Planning Commission (202240110), and National Key R&D Program of China (62373243).

References

- [1] Nikolas Lessmann, Bram Van Ginneken, Pim A De Jong, and Ivana Išgum. Iterative fully convolutional neural networks for automatic vertebra segmentation and identification. *Medical image analysis*, 53:142–155, 2019.
- [2] Joseph E Burns, Jianhua Yao, Hector Muñoz, and Ronald M Summers. Automated detection, localization, and classification of traumatic vertebral body fractures in the thoracic and lumbar spine at ct. *Radiology*, 278(1):64–73, 2016.
- [3] Dejan Knez, Boštjan Likar, Franjo Pernuš, and Tomaž Vrtovec. Computer-assisted screw size and insertion trajectory planning for pedicle screw placement surgery. *IEEE transactions on medical imaging*, 35(6):1420–1430, 2016.
- [4] Jack C Cheng, René M Castelein, Winnie C Chu, Aina J Danielsson, Matthew B Dobbs, Theodoros B Grivas, Christina A Gurnett, Keith D Luk, Alain Moreau, Peter O Newton, et al. Adolescent idiopathic scoliosis. *Nature reviews disease primers*, 1(1):1–21, 2015.
- [5] Hendrik Möller, Robert Graf, Joachim Schmitt, Benjamin Keinert, Matan Atad, Anjany Sekuboyina, Felix Streckenbach, Hanna Schön, Florian Kofler, Thomas Kroencke, et al. Spineps—automatic whole spine segmentation of t2-weighted mr images using a two-phase approach to multi-class semantic and instance segmentation. *arXiv preprint arXiv:2402.16368*, 2024.
- [6] Maximilian T Löffler, Anjany Sekuboyina, Alina Jacob, Anna-Lena Grau, Andreas Scharr, Malek El Husseini, Mareike Kallweit, Claus Zimmer, Thomas Baum, and Jan S Kirschke. A vertebral segmentation dataset with fracture grading. *Radiology: Artificial Intelligence*, 2(4):e190138, 2020.
- [7] Xin You, Yun Gu, Yingying Liu, Steve Lu, Xin Tang, and Jie Yang. Verteformer: A single-staged transformer network for vertebrae segmentation from ct images with arbitrary field of views. *Medical Physics*, 2023.
- [8] Tobias Klinder, Jörn Ostermann, Matthias Ehm, Astrid Franz, Reinhard Kneser, and Cristian Lorenz. Automated model-based vertebra detection, identification, and segmentation in ct images. *Medical image analysis*, 13(3):471–482, 2009.
- [9] Kerstin Hammernik, Thomas Ebner, Darko Stern, Martin Urschler, and Thomas Pock. Vertebrae segmentation in 3d ct images based on a variational framework. *Recent advances in computational methods and clinical applications for spine imaging*, pages 227–233, 2015.
- [10] Poay Hoon Lim, Ulas Bagci, and Li Bai. A robust segmentation framework for spine trauma diagnosis. In *Computational Methods and Clinical Applications for Spine Imaging: Proceedings of the Workshop held at the 16th International Conference on Medical Image Computing and Computer Assisted Intervention, September 22-26, 2013, Nagoya, Japan*, pages 25–33. Springer, 2014.
- [11] Melih S Aslan, Asem Ali, Dongqing Chen, Ben Arnold, Aly A Farag, and Ping Xiang. 3d vertebrae segmentation using graph cuts with shape prior constraints. In *2010 IEEE ICIP*, pages 2193–2196. IEEE, 2010.
- [12] Xin You, Yun Gu, Yingying Liu, Steve Lu, Xin Tang, and Jie Yang. Eg-trans3dunet: a single-staged transformer-based model for accurate vertebrae segmentation from spinal ct images. In *ISBI*, pages 1–5. IEEE, 2022.
- [13] Di Meng, Edmond Boyer, and Sergi Pujades. Vertebrae localization, segmentation and identification using a graph optimization and an anatomic consistency cycle. *Computerized Medical Imaging and Graphics*, 107:102235, 2023.

- [14] Naoto Masuzawa, Yoshiro Kitamura, Keigo Nakamura, Satoshi Iizuka, and Edgar Simo-Serra. Automatic segmentation, localization, and identification of vertebrae in 3d ct images using cascaded convolutional neural networks. In *Medical Image Computing and Computer Assisted Intervention–MICCAI 2020: 23rd International Conference, Lima, Peru, October 4–8, 2020, Proceedings, Part VI 23*, pages 681–690. Springer, 2020.
- [15] Rong Tao, Wenyong Liu, and Guoyan Zheng. Spine-transformers: Vertebra labeling and segmentation in arbitrary field-of-view spine cts via 3d transformers. *Medical Image Analysis*, 75:102258, 2022.
- [16] Christian Payer, Darko Stern, Horst Bischof, and Martin Urschler. Coarse to fine vertebrae localization and segmentation with spatialconfiguration-net and u-net. In *VISIGRAPP (5: VISAPP)*, pages 124–133, 2020.
- [17] Özgün Çiçek, Ahmed Abdulkadir, Soeren S Lienkamp, Thomas Brox, and Olaf Ronneberger. 3d u-net: learning dense volumetric segmentation from sparse annotation. In *MICCAI 2016: 19th International Conference, 2016, Proceedings, Part II 19*, pages 424–432. Springer, 2016.
- [18] Anjany Sekuboyina, Malek E Hussein, Amirhossein Bayat, Maximilian Löffler, Hans Liebl, Hongwei Li, Giles Tetteh, Jan Kukačka, Christian Payer, Darko Štern, et al. Verse: a vertebrae labelling and segmentation benchmark for multi-detector ct images. *Medical image analysis*, 73:102166, 2021.
- [19] Han Wu, Jiadong Zhang, Yu Fang, Zhentao Liu, Nizhuan Wang, Zhiming Cui, and Dinggang Shen. Multi-view vertebra localization and identification from ct images. In *International Conference on Medical Image Computing and Computer-Assisted Intervention*, pages 136–145. Springer, 2023.
- [20] Fabian Isensee, Paul F Jaeger, Simon AA Kohl, Jens Petersen, and Klaus H Maier-Hein. nnu-net: a self-configuring method for deep learning-based biomedical image segmentation. *Nature methods*, 18(2):203–211, 2021.
- [21] Yucheng Tang, Dong Yang, Wenqi Li, Holger R Roth, Bennett Landman, Daguang Xu, Vishwesh Nath, and Ali Hatamizadeh. Self-supervised pre-training of swin transformers for 3d medical image analysis. In *CVPR*, pages 20730–20740, 2022.
- [22] Saikat Roy, Gregor Koehler, Constantin Ulrich, Michael Baumgartner, Jens Petersen, Fabian Isensee, Paul F Jaeger, and Klaus H Maier-Hein. Mednext: transformer-driven scaling of convnets for medical image segmentation. In *MICCAI*, pages 405–415. Springer, 2023.
- [23] Enze Xie, Peize Sun, Xiaoge Song, Wenhai Wang, Xuebo Liu, Ding Liang, Chunhua Shen, and Ping Luo. Polarmask: Single shot instance segmentation with polar representation. In *CVPR*, pages 12193–12202, 2020.
- [24] Wonhui Park, Dongkwon Jin, and Chang-Su Kim. Eigencontours: Novel contour descriptors based on low-rank approximation. In *Proceedings of the IEEE/CVF Conference on Computer Vision and Pattern Recognition*, pages 2667–2675, 2022.
- [25] Eric W Weisstein. Spherical coordinates. <https://mathworld.wolfram.com/>, 2005.
- [26] William E Lorensen and Harvey E Cline. Marching cubes: A high resolution 3d surface construction algorithm. In *Seminal graphics: pioneering efforts that shaped the field*, pages 347–353. 1998.
- [27] Will Schroeder, Kenneth M Martin, and William E Lorensen. *The visualization toolkit an object-oriented approach to 3D graphics*. Prentice-Hall, Inc., 1998.
- [28] Jeya Maria Jose Valanarasu and Vishal M Patel. Unext: Mlp-based rapid medical image segmentation network. In *MICCAI 2022, Singapore, Proceedings, Part V*, pages 23–33. Springer, 2022.
- [29] Varduhi Yeghiazaryan and Irina Voiculescu. Family of boundary overlap metrics for the evaluation of medical image segmentation. *Journal of Medical Imaging*, 5(1):015006–015006, 2018.